Rare Metal Materials and Engineering
Volume
Available online at **www.rmme.ac.cn**

Science Press

Cite this article as: Rare Metal Materials and Engineering,

ARTICLE

https://doi.org/10.12442/j.issn.1002-185X.20260014

The fracture mechanism and fatigue stress prediction model of nickel-based single-crystal high-temperature alloys under high-cycle fatigue conditions

Zhen Li[1, 2,3,4], **Yuanming Xu** [2], **xinling Liu** [1,3,4], **xing Chen** [1,3,4], **Changkui Liu** [1,3,4]

[1] AECC Beijing Institute of Aeronautical Materials, Beijing 100095, China; [2] School of Aeronautic Science and Engineering, Beihang University, Beijing 100191, China; [3]AECC/AVIC Failure Analysis Center, Beijing 100095, China; [4]ABeijing Key Laboratory of Aeronautical Materials Testing and Evaluation, Beijing 100095, China

Abstract: High-temperature and high-cycle fatigue tests have been conducted on nickel-based single crystal superalloys at 760 ℃ and 850 ℃. The macroscopic and microscopic features of the high-cycle fatigue fracture surfaces were assessed by optical and scanning electron microscopy. Fatigue crack propagation tests were conducted to establish the stable propagation characteristics. In addition, a new quantitative analysis parameter for fatigue fracture and a fatigue stress prediction model are proposed and applied in the prediction of high-cycle fatigue stress effects. The errors associated with different models are calculated and compared. The results demonstrate that, at 760 ℃ and 850 ℃ and a stress ratio (R) of 0.05 and -1, the location of high-cycle fatigue crack initiation, the propagation direction, and the fracture surface characteristics are similar, presenting typical staged characteristics. The cracks all originate from internal porosity and material voids. The early stage of the crack propagation zone exhibits smooth and flat crystallographic plane characteristics. At the later stage, the crack propagation zone shows "brittle fatigue band" characteristics. The fracture surface is inclined at a certain angle to the loading direction, generating a composite crack. The brittle fatigue band features of the nickel-based single crystal alloys are significantly different from those associated with steel and aluminum polycrystalline alloys in terms of morphology and spacing size order of magnitude. Based on the stable propagation characteristics of the fatigue cracks, the parameters required for the fatigue stress prediction model were calculated. The crack shape factor "cylindrical semi-elliptical surface crack" was selected. This factor reflects the initiation and propagation direction of the fatigue cracks. Based on this, the correction coefficient for the composite crack shape factor, which represents the characteristics of the alloy inclined cracks, was calculated. Conventional Paris and Forman models that incorporate the stress ratio and fracture toughness (K_C) were selected as the fatigue stress prediction models. The predicted results are compared with the nominal stress, with a prediction error for the Paris model between 1.0 and 1.9, and between 1.05 and 1.30 in the case of the Forman model. The results indicate that accurate fatigue stress prediction requires the selection of prediction parameters and models which match the fatigue fracture characteristics.

Key words: Ni-based single crystal superalloy; High cycle fatigue; Crack initiation mechanism; Brittle fatigue striations; Crack form factor; Prediction of fatigue stress magnitude; Quantitative analysis of fatigue fracture; Damage tolerance design

The fatigue fracture of materials can be classified as low-cycle (<10^4 cycles), high-cycle (10^4-10^7 cycles), and ultra-high-cycle (>10^7 cycles) based on the number of times the components are subjected to a load. In the stress analysis and determination of low-cycle failure, the component stress can be calculated using force analysis and finite element simula-

Received date:
Foundation item: NSFC(××××)
Corresponding author: ×××, Ph.D., Professor, Rare Metal Material and Engineering Press, Northwest Institute for Nonferrous Metal Research, Xi'an 710016, P. R. China, Tel: 0086-29-86231117, E-mail: rmme@c-nin.com

tion, or by applying experimental methods. It is difficult to conduct a force analysis in the case of a vibration load or high-cycle fatigue load borne by high-speed rotating parts. Nevertheless, high-cycle fatigue fracture is quite common in engineering practice[1]. The quantitative analysis of fatigue fracture employs the characteristics of the fatigue fracture formed following component fracture to reverse analyze and calculate the stress magnitude and history, and predict the remaining lifespan. It has been successfully applied in multi-crystalline materials such as steel and aluminum, providing valuable support for failure analysis and fault detection in engineering practice. The typical fatigue band characteristics of aluminum alloy and steel are illustrated in Fig. 1(a) and 1(b).

The high-cycle fatigue of nickel-based single-crystal superalloys exhibits typical staged characteristics. Cracks principally originate from the internal porosity. In the early stage of fatigue crack propagation (denoted in this study as the “first stage”), the characteristics are similar to cleavage slip, and no fatigue band features are observed. We have developed a fatigue stress prediction method for cleavage slip, which was applied to the first stage of fatigue crack propagation. A prediction error similar to that of polycrystalline materials[2] was achieved using the parameters associated with the "crack tip plastic zone" based on fracture mechanics and combining the inverse calculation of the composite crack shape factor for the high-cycle fatigue stress. However, in the later stage of single crystal high-temperature alloy expansion (denoted as the “second stage”), the brittle fatigue band feature was also observed, as shown in Fig. 1(c). This fatigue feature in single crystal high-temperature alloys differs somewhat from the fatigue bands of conventional steels, aluminum and titanium alloys. The fatigue is mainly manifested in the plastic nature of the band morphology, wide band spacing, fast crack propagation rate, a difference in magnitude compared with multi-crystalline materials, and rapid growth as the crack develops. Currently, there is no reported study that has utilized the "brittle fatigue band" feature to predict the fatigue stress of single crystal high-temperature alloys.

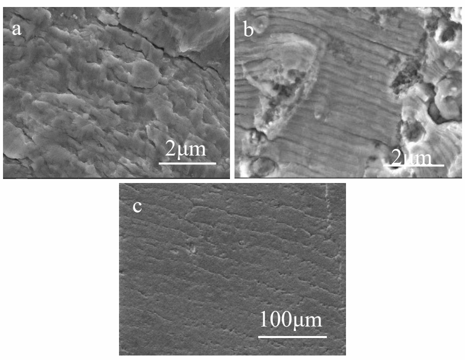

Fig. 1 (a) Fatigue strip characteristics of the 35Cr2Ni4MoA high-strength alloy steel; (b) Fatigue strip characteristics of the 7050 aluminum alloy; (c) Image showing the characteristics of brittle fatigue bands in nickel-based single-crystal high-temperature alloys

The stress magnitude that a component has endured is typically predicted by a reverse calculation based on the characteristics of fatigue bands, applying the classic Paris model[2], using Equation (1). In a quantitative analysis and prediction of fatigue stress fractures, researchers have examined the influence of the shape factor, crack propagation material constant, and the measurement error associated with fatigue band spacing. The quantitative analysis of fatigue stress fractures has been applied under constant amplitude loading and simple cracking forms of component failure, such as bolt fatigue fracture stress. In the case of the bending vibration fatigue fracture of compressor blades, quantitative analysis and prediction have delivered good results. However, an in-depth and systematic evaluation of the reverse calculation of stress from fracture under complex stress shape factors and complex load spectra is required to facilitate meaningful applications.

$$\frac{\mathrm{d}a}{\mathrm{d}N} = c(\Delta K)^n \tag{1}$$

Xu[3] has revealed that the optimal high-cycle fatigue performance of a fourth-generation nickel-based single crystal superalloy is obtained at 980 °C, followed by 700 °C and 850 °C. This was attributed to the transition of dominant micro-deformation mechanisms with increasing temperature from stacking fault locks and Lomer-Cottrell dislocations to cross-slip, and ultimately to intense dislocation activities including Kear-Wilsdorf locks, pile-ups, and entanglements. Zhou[4] investigated the failure mechanisms of three different crystal orientations of single-crystal high-temperature alloys during the entire high-temperature and low-cycle fatigue process. Zhang[5] has shown that the low-cycle fatigue crack initiation behavior of a nickel-based single crystal superalloy at 530 °C is governed by the maximum strain. Yang *et al*[6] conducted research on the low-cycle fatigue fracture behavior of the shot-peened GH738 alloy at 650 °C. They proposed a quantitative fatigue fracture analysis model suitable for deformation of high-temperature alloys. Zhang and co-workers[7] reported a simple and feasible method of assessing the vibration stress of blades by utilizing the fatigue band spacing that exhibited small errors. Li *et al.*[8] employed fatigue band characteristics to obtain the relationship between the crack propagation rate (da/dN) and the amplitude (ΔK) of the crack stress intensity factor, and determined the magnitude of the vibration stress of rotating blades. Moreover, Zheng *et al*[9] applied the Paris formula to establish the initial fatigue quality of a welded structure, which exhibited a normal distribution. The experimental results have significant engineering significance in the process qualification of titanium alloy electron beam welded structures. Chen and co-workers[10] used the fatigue band characteristics to quantitatively analyze and predict the fatigue fracture stress of rivets. They showed that the combined initial fatigue stress was large, whereas the expansion stress was small. With the development of artificial intelligence, Tan L[11] applied neural networks and the theory of crystal plastic slip to predict the high-cycle fatigue life of single crystal alloys.

The Paris model does not take into account the influence of parameters such as stress ratio and fracture toughness on the crack propagation behavior of materials. As different materials exhibit different crack propagation characteristics, the stress analysis calculation model must be modified according to the particular application. The fracture characteristics of single-crystal high-temperature alloys under high-cycle fatigue deviate significantly from those of Al alloys and polycrystalline steel alloys. The applicability of the fatigue analysis parameters requires a comprehensive assessment. A range of experimental studies have been conducted to correct the influence of the near-threshold and high-speed propagation regions on the crack propagation rate, and modifications to the Paris formula have been proposed. In 1972, Forman proposed a modified formula:

$$\frac{\mathrm{da}}{\mathrm{dN}} = \frac{\mathrm{c}(\Delta \mathrm{K})^n}{(1-R)K\mathrm{c} - \Delta \mathrm{K}} \tag{2}$$

The Forman formula takes into account the influence of the cyclic stress ratio (R) and fracture toughness (K_c). The R values vary under different average stresses, and the Forman formula can accurately express the load conditions under a particular cyclic R value. The formula has been widely applied in the development of crack propagation data tables for high-strength steels and aluminum alloys. To date, there have been no reported studies that have utilized this model in the reverse prediction of fatigue stress at the fracture surface. Furthermore, current methods based on plastic striations and the assumption of Mode-I are not applicable to nickel-based single crystal alloys.

This study sets out to clarify the formation mechanism of the "brittle fatigue zone" and establish a complete quantitative prediction method for fatigue stress fracture based on the characteristics of the "brittle fatigue zone". Moreover, we provide a comparison with fatigue stress models for conventional polycrystalline alloys, with an analysis of the sources of errors and model applicability. This study builds on and significantly extends prior work in developing fatigue stress prediction methods for single crystal high-temperature alloys. The findings of this research provide the basis for a reliable calculation of the actual failure load of engine blades and the improvement of the material lifespan.

1 Experiment

1.1 Materials

The [001] direction of second-generation single-crystal high-temperature alloy was selected in this study; the chemical composition is given in Table 1. Figure 2(a) illustrates the casting method for the rod and sheet materials, which used a directional solidification furnace with the helical selection crystal method. The pulling rate was maintained at 3.5-4 mm/min, ensuring continuity of crystal growth, and the deviation from the [001] direction orientation was controlled within 10° by applying the Laue method. Subsequently, a standard heat treatment was carried out: 1290 ℃/1 h + 1300 ℃/2 h + 1315 ℃/4 h/Air Cooling(AC) + 1120 ℃/4 h/AC + 870 ℃/32 h/AC.

Table 1 Chemical composition (mass fraction,%) of the nickel-based single crystal superalloy

C	Cr	Co	W	Mo	Al
0.01-0.04	3.8-4.8	8.5-9.5	7.0-9.0	1.5-2.5	5.2-6.2
Hf	Ta	Nb	Re	Ni	
0.05-0.15	6.0-8.5	0.8-1.2	1.6-2.4	Balance	

The metallographic structure and morphology of the strengthening phase γ' (Ni_3Al) of the material following heat treatment are shown in Fig. 2(b). Dendrite segregation is evident, and the strengthening phase is regular and ordered.

1.2 High-cycle fatigue and crack propagation samples

The high-cycle fatigue rod-shaped samples were processed using mechanical methods. The length direction of the sample was parallel to the [001] direction. The working section exhibited non-uniform cross-sectional dimensions and was processed by longitudinal polishing to achieve a roughness of Ra ≤ 0.4. This served to eliminate the influence of surface processing damage on fatigue life, as shown in Fig. 3.

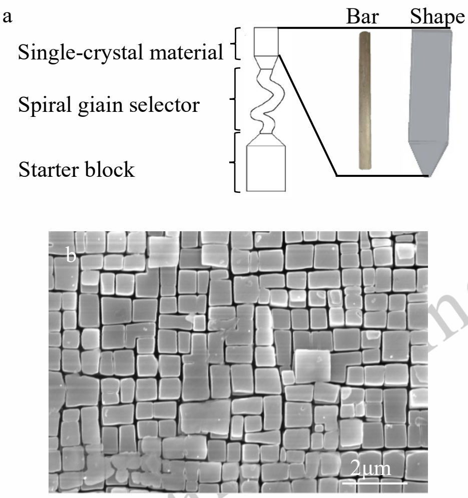

Fig. 2 (a) Casting method used in the preparation of nickel-based single-crystal superalloys; (b) enhanced phase (γ' -Ni3Al) morphology

Crack propagation experiments were conducted to generate the crack characteristics and parameters (C and n) during the stable fatigue crack propagation process. This provided fundamental data for the fatigue stress prediction model of single crystal alloys based on fatigue bands.

A schematic representation of the common crack propagation modes associated with turbine blades under actual operating conditions is presented in Fig. 4(a). The high-pressure turbine blades grow in the [001] direction. During operation, the blades mainly bear centrifugal force and bending moments, and cracks tend to form in the blade body and extend perpendicularly to the height direction of the blade. The samples were cut in the [001] direction perpendicular to the casting, as shown in Fig. 4(b). This ensured that the fatigue crack propagation test samples bore loads consistent with the crack propagation direction and the actual blade loads. When the stress ratio (R) > 0, the C-T type compact tensile samples were used. The rack opening direction was consistent with the [001] direction perpendicularly, with a sample thickness (B) = 10 mm (Fig. 4(c)). When R < 1, the M-T type compact sample was used to ensure the application of a reverse compression load, as shown in Fig. 4(d) and 4(e).

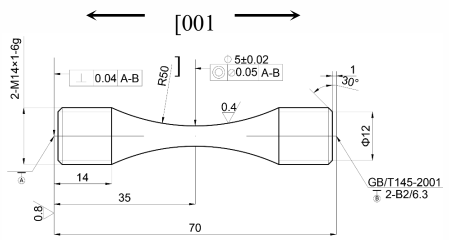

Fig. 3 High-frequency fatigue sample processing dimensions

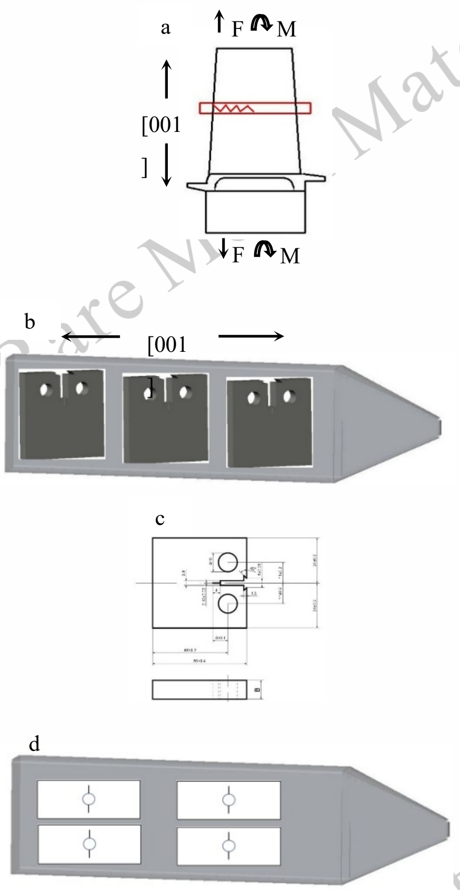

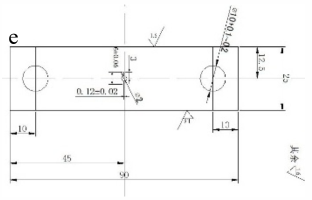

Fig. 4 (a) Schematic representation of the load on turbine blades and consequent cracking; (b) Representation of the C-T sample for testing at R > 0; (c) Dimensions of the C-T sample; (d) Representation of the M-T sample for testing at R < 0; (e) Dimensions of the M-T sample

1.3 High-cycle fatigue testing

The main working temperature range of single crystal high-temperature alloys in engines is from 760 ℃ to 980 ℃, where 760 ℃ and 850 ℃ served as two typical operating temperature points. High-cycle fatigue tests were conducted at different temperatures and stress ratios to ensure a comprehensive assessment and prediction of the fatigue fracture characteristics of single crystal high-temperature alloys in the engine operating temperature range. The operating conditions are presented in Table 2. A QBG-200 high-cycle fatigue testing machine (Qianbang) was employed with furnace heating, a sinusoidal load waveform and 110 Hz test frequency, applying the load-controlled mode.

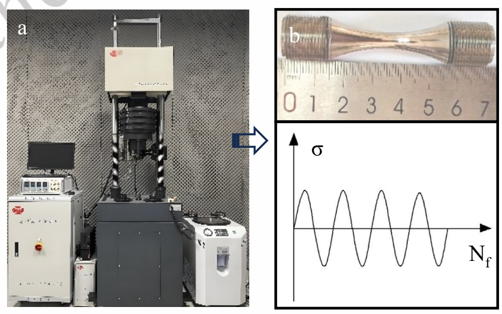

Fig. 5 (a) High-cycle fatigue testing unit, and (b) test load waveform

Table 2 High-cycle fatigue testing conditions

Temperature/ ℃	Stress ratio/R
850	0.05, -1
760	0.05, -1

1.4 Fatigue crack propagation testing

The crack propagation experiments at different temperatures (760 ℃ and 850 ℃) were conducted using the MTS370 microcomputer-controlled fatigue testing machine. The samples were heated in a furnace, applying a sine wave load waveform and a frequency of 10 Hz (Fig. 6), and using the load-controlled mode. The experimental procedures complied with the HB7680-2000 requirements: "Experimental Method for High Temperature Fatigue Crack Propagation Rate of Metallic Materials"[12].

Before the experiment, the thickness, notch length, and width of the processed sample were measured. The load was set according to the sample size. A pre-crack was formed before collecting the stable crack propagation data, where the load size was adjusted so the stable crack propagation rate reached 10^{-5} mm/cycle. The potential method was employed to record the corresponding number of cycles (N) at a particular crack length. Data processing enabled a calculation of the crack propagation rate (da/dN) and the stress intensity factor range (ΔK).

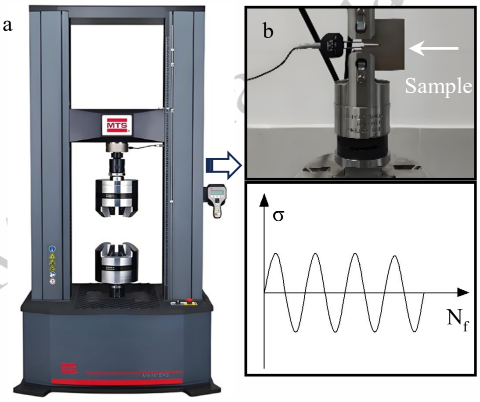

Fig. 6 (a) Fatigue crack propagation test unit, and (b) test load waveform

Table 3 Experimental conditions and samples used in metal fatigue crack propagation testing

Temperature/ ℃	Stress ratio/R	Sample type
760, 850	0.05	C-T
760, 850	-1	M-T

1.5 Prediction of fatigue stress

1. Fatigue crack path monitoring and damage mechanism analysis

The macroscopic morphology of the fatigue fracture surface was monitored using an Olympus DSX110X stereomicroscope (Olympus, Tokyo, Japan) to determine the location of crack initiation, the direction of the main crack propagation, and the arc-shaped features of the fracture surface. A GEMiNi300 (Carl Zeiss AG, Jena, Germany) Zeiss field emission scanning electron microscope (SEM) was utilized for microscopic analysis of the crack source and extension areas. A FEI Talos F200S (Fortress Energy Incorporated, Hillsboro, OR, USA) HADDF function was employed to characterize the fracture surface and composition distribution. The high-resolution mode was used to characterize the morphology, composition, and dislocation configuration of the fracture surface and matrix[13].

2. Monitoring and measurement of brittle fatigue bands

The fatigue strip morphology of the fatigue fracture was monitored and the fatigue strip spacing measured using the GEMiNi300 SEM unit, applying the following three steps. (1) Low-magnification observation of the overall fracture morphology was conducted to determine the location and end position of the fatigue strip and the main crack propagation path. The starting position of the fatigue strip, the end position of the first stage, the starting position of the second stage, and the end position of the fatigue strip occurred at the completion of crack propagation. (2) The source area position was located and the coordinates recorded. (3) Returning to the first measurement point position, the coordinates were recorded with image processing to measure the fatigue strip spacing. The image size was sufficiently large to clearly display the fatigue strip morphology and facilitate measurement. The three steps were repeated along the crack propagation path until the measurement was completed. Data from at least four measurement points were obtained for each sample. The distance from the measurement point to the crack source area was calculated from the coordinates, and the crack lengths (a) and fatigue strip spacing (*i.e.*, the crack propagation rate (da/dN)) associated with the crack length are given in Table 4.

Table 4 Measurement results for the fatigue stripes on the fracture surface (D1H230)

a/m	da/dN/mm
0.001142804	0.02500
0.001232234	0.05200
0.001336759	0.06845
0.001441284	0.08090
0.001519704	0.08690
0.001598124	0.09089

3. Application of the fracture shape factor

The crack shape factor represents the morphology of the crack leading edge during crack extension and is an essential parameter in fatigue stress prediction. The selection of the crack shape factor is based on sample geometry, the location of crack initiation, and the extension path. The sample used was cylindrical with a circular cross-section. The "cylindrical semi-elliptical surface crack" model in the "Stress Intensity Factor Handbook" serves as the classic model for describing surface or near-surface defects on cylindrical bodies. Under high-cycle fatigue, crack initiation and extension in the smooth cylindrical nickel-based single crystal superalloy originate from surface or subsurface casting defects and expand into the material on both sides. This expansion process generates a semi-elliptical contour on a macroscopic scale. All these features are consistent with the boundary conditions of the model.

A parametric treatment has established a binary quadratic mathematical model suitable for engineering applications. The characteristics relating to inclined crack fracture are evaluated to determine the composite crack shape factor.

Equation 3 was used to calculate the crack shape factor, where E(k) denotes the second elliptic integral, calculated using Equation 4. The correction factor (F_{I}) values, given in Table 5[14], represent a discontinuous sequence of numerical data. The tabulated values are mathematically modeled to improve applicability in engineering contexts, as illustrated in equation

5. The correction factor (F_I) is associated with the parameters c/D and c/b. A bivariate quadratic function that incorporates interaction terms is employed to accurately represent the relationships between these parameters and F_I, as expressed in equation 6. Where x_1 = c/D and x_2 = c/b, the relevant expression for F_I is given by Equation 7.

$$Y_I = \frac{F_I}{E(k)} \tag{3}$$

$$E(k) = \left[1 + 1.464\left(\frac{c}{b}\right)^{1.65}\right]^{1/2} \quad c/b \le 1 \tag{4}$$

$$F_I = m_0 + m_1 x_1 + m_2 x_2 + m_3 x_1 x_2 + m_4 x_1^2 + m_5 x_2^2 \tag{5}$$

The m_0-m_5 factors are constants. A regression analysis was conducted on the bivariate quadratic function to derive Equation 6. Where F (119.84) exceeds the significance F value (5.92×10^{-8}), the associated larger difference corresponds to a more significant correlation in terms of the regression equation. A comparison of the fitted and actual values has an absolute error range of 0.65%-4.13%, indicating a relatively small error margin and reliable results.

$$F_I = 1.81 + 3.48x_1 - 2.10x_2 - 4.82x_1x_2 + 4.32x_1^2 + 1.40x_2^2 \tag{6}$$

$$Y_I = \frac{1.81 + 3.48x_1 - 2.10x_2 - 4.82x_1x_2 + 4.32x_1^2 + 1.40x_2^2}{\sqrt{1 + 1.464(x_2)^{1.65}}} \tag{7}$$

Table 5 Values of the correction factor (F_I)

c/D	c/b=1	c/b=0.8	c/b=0.6
0.05	1.012	1.056	1.107
0.125	1.015	1.083	1.176
0.2	1.038	1.131	1.316
0.275	1.087	1.227	1.565
0.35	1.175	1.387	1.835

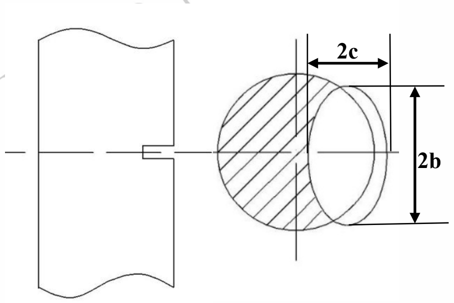

Fig. 7 Schematic representation of the cylindrical semi-elliptical surface crack model

The local perturbation method and variance-based Sobol global sensitivity analysis were employed to evaluate the sensitivity of the crack shape factor model to the input parameters. The results presented in Table 6 and Fig. 8 establish the following: (1) c/b is the dominant sensitive crack shape factor parameter, and an accurate measurement determines the stress prediction error; (2) the model exhibits significant nonlinear characteristics ($\Sigma S\_Ti = 1.093 > 1$), and the interaction effect contributes approximately 9.3% of the output variance; (3) the response surface and contour plots confirm that, where c/D > 0.4 and c/b < 0.6, the shape factor is sensitive to parameter changes. In engineering applications, the accuracy of c/b should be prioritized for calibration. Moreover, in the later stage of crack propagation, a complete binary quadratic model must be adopted rather than a simplified linear model. In terms of contour plots, the finding provides a quantitative basis for the damage tolerance design of single crystal blades.

Table 6 Sobol global sensitivity index

Parameters	First-order exponent S_i	95% Confidence Interval	Total order index S_{Ti}	95% Confidence interval
c/D	0.215	[0.188,0.242]	0.308	[0.276,0.340]
c/b	0.692	[0.661,0.723]	0.785	[0.749,0.821]
Interaction	S_{12}=0.093	-	-	-

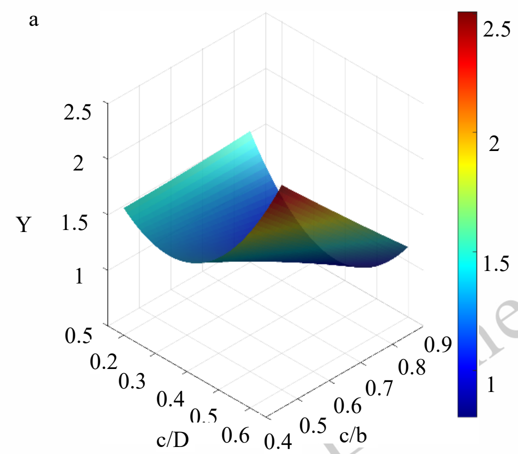

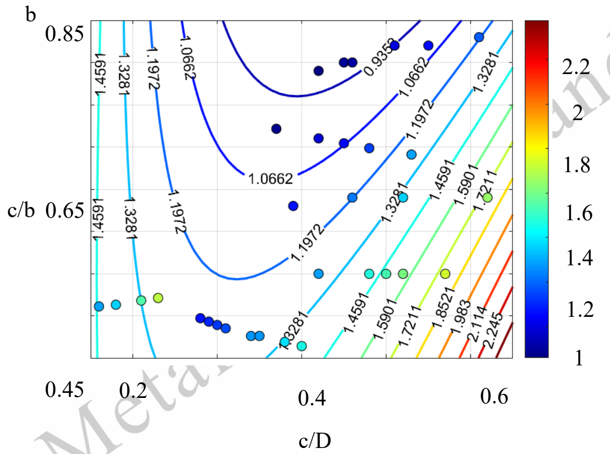

Fig. 8 (a) Composite crack shape factor response surface; (b) contour maps and distribution maps for the measured data

4. Prediction of fatigue stress

As outlined in section 2.4, the steady-state crack propagation parameters required for the fatigue stress prediction model were obtained from fatigue crack propagation experiments. Moreover, the fracture characteristics and parameters needed for the fatigue stress prediction were determined by applying the procedures outlined above. A fatigue stress prediction model was selected based on the fatigue crack propagation characteristics of the nickel-based single crystal alloy. The Paris and Forman models were used to correlate the crack propagation rate (brittle fatigue band) with the stress intensity factor (K). The crack propagation rate was established from the relationship between the stress intensity factor and the fatigue stress. The fatigue stress prediction effects obtained from the Paris and Forman models are compared to determine the stress prediction model that best matches the high-cycle fatigue of single crystal superalloys. The overall procedural flowchart is presented in Fig. 9.

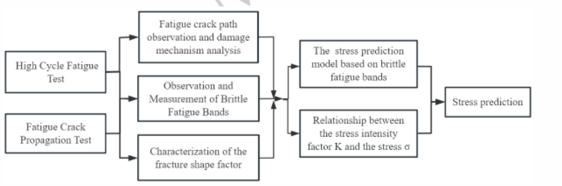

Fig. 9 Framework for fatigue stress prediction.

2 Results and Discussion

2.1 High-cycle fatigue life

The results of high-cycle fatigue tests on the single crystal superalloy at 760 °C and 850 °C (R = -1) are presented in Fig. 10(a). The maximum stress (σ_{max}) ranges from 340 MPa to 450 MPa, and the lifespan is distributed between 10^5 and 10^7 cycles. As the σ_{max} is increased, the high-cycle fatigue life (N_f) exhibits a gradual decrease, which is consistent with the reported response of polycrystalline materials[12][13]. The results of high-cycle obtained where R = 0.05 are given in Fig. 10(b). In this case, σ_{max} ranges from 580 MPa to 660 MPa, and the lifespan is distributed between 10^5 and 2×10^7 cycles. The increase in σ_{max} is accompanied by a decrease in N_f[15].

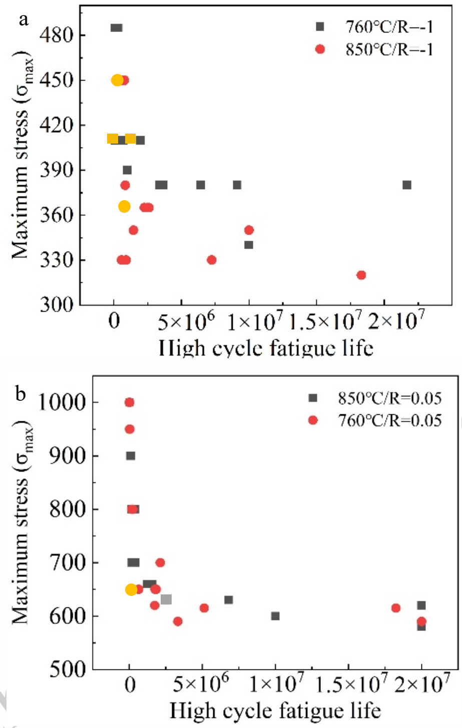

Fig. 10 (a) High-cycle fatigue life results at R = -1 (the analyzed samples are marked in yellow); (b) High-cycle fatigue life at R = 0.05 (the analyzed samples are marked in yellow).

2.2 High-cycle fatigue fracture behavior and fracture surface morphology characteristics

The macroscopic morphologies of the high-cycle fatigue fracture surfaces at 760 °C and 850 °C are shown in Fig. 11, where R = 0.05. The fracture surfaces at both temperatures are consistently at an angle to the direction of load application, forming oblique cracks. The statistical results are presented in Table 7. Based on the convergence direction of the extended edges, the cracks originate from the internal surface or near the surface of the material. Distinct "fish-eye" color boundary features can be observed near the crack source area. In the early stage of the expansion zone, there is evidence of smooth and flat crystallographic plane features. In contrast, fatigue strip features are apparent in the later stage of the expansion zone. The corresponding high-cycle fatigue fracture surface morphologies at R = -1 are presented in Fig. 12. The fracture surface characteristics are similar to those observed at R = 0.05. Typical stage-specific features can be seen, with the appearance of fatigue strips in the second stage of fatigue expansion.

Representative SEM images, showing the characteristics of the fatigue bands, are presented in Fig.13 and 14. A preliminary measurement of the fatigue band spacing was conducted. The results indicate that, at R = 0.05 and R = -1 (and 760 ℃

and 850 ℃), the spacing increases with increasing crack length. This is consistent with the patterns observed for steel and aluminum alloys, but the growth rates differ.

The high-magnification images of the fracture surfaces (Fig. 15 and 16) exhibit corundum-like morphology. The associated energy spectrum indicates a certain degree of oxidation. The principal elemental components of the fracture surface are O, Al, and Ni. The thickness of the oxidation layer at 850 °C is significantly higher than that recorded at 760 °C. The treatment temperature has a significant impact on the degree of fracture oxidation, as shown in Table 8. The characteristics with respect to different stress ratios at the same temperature are not obvious. At 850 °C, the stress ratio R = -1 is higher than R = 0.05. The thickness of the oxidation layer varies at different crack lengths for the same sample, and the oxidation layer thickness in the crack propagation zone is significantly higher than that in the crack initiation zone.

Table 7 The angle between the fracture surface and the direction of the applied load

Sample label	Measuring angle/°
D6H202	50
D1H230	56
D6H203	55
D6H207	60
D6H229	57
D6H236	53

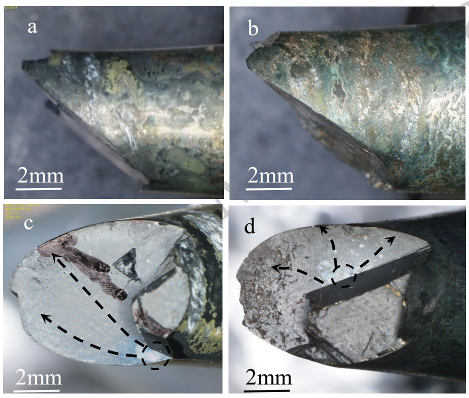

Fig. 11 (a) Oblique crack fracture morphology of sample D6H202 (760 ℃/R = 0.05, σ_{max}= 650 MPa); (b) Oblique crack fracture morphology of sample D1H230 (850 ℃/R = 0.05, σ_{max} = 660 MPa); (c) Crack initiation and propagation direction for sample D6H202; (d) Crack initiation and propagation direction for sample D1H230

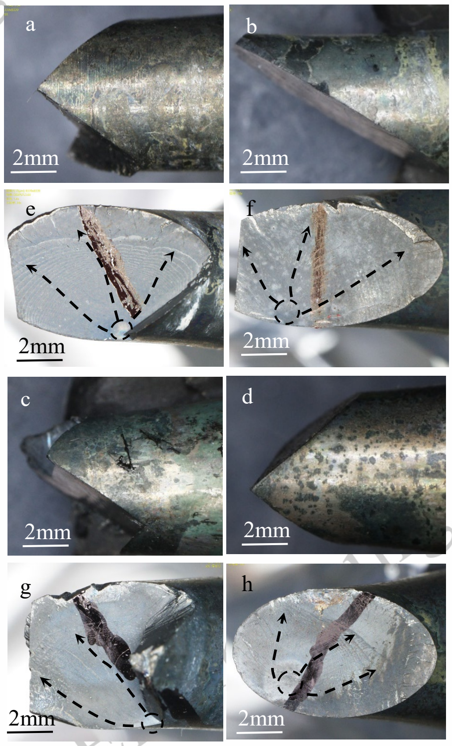

Fig. 12 (a) Oblique crack fracture morphology of sample D6H203 (760 ℃/R= -1, σ_{max} = 410 MPa); (b) Oblique crack fracture morphology of sample D6H207 (760 ℃/R = -1, σ_{max} = 410 MPa); (c) Oblique crack fracture morphology of sample D6H229 (850 ℃/R = -1, σ_{max} = 450 MPa); (d) Oblique crack fracture morphology of sample D6H236 (850 ℃/R = -1, σ_{max} = 365 MPa); (e) Crack initiation and propagation direction of sample D6H203; (f) Crack initiation and propagation direction of sample D6H207; (g) Crack initiation and propagation direction of sample D6H229; (h) Crack initiation and propagation direction of sample D6H236

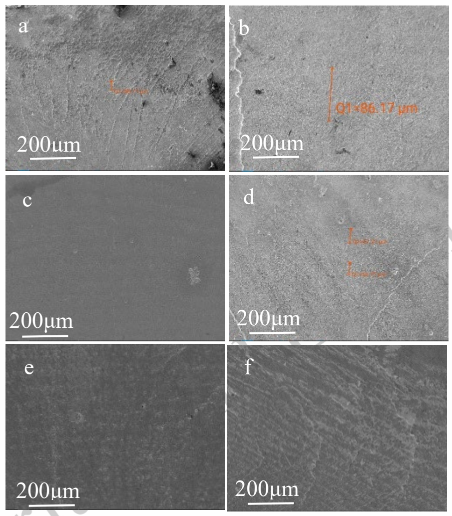

Fig. 13 Surface morphology of the second stage of crack propagation in (a) sample D1H230 (850 ℃/R = 0.05, σ_{max} = 660 MPa), (b) sample D6H202 (760 ℃/R = 0.05, σ_{max} = 650 MPa), (c) sample D6H203 (760 ℃/R = -1, σ_{max} = 410 MPa), (d) sample (760 ℃/R = -1, σ_{max} = 410 MPa), (e) sample D6H229 (850 ℃/R = -1, σ_{max} = 450 MPa), and

(f) sample D6H229 (850 ℃/R = -1, σ_{max} = 365 MPa)

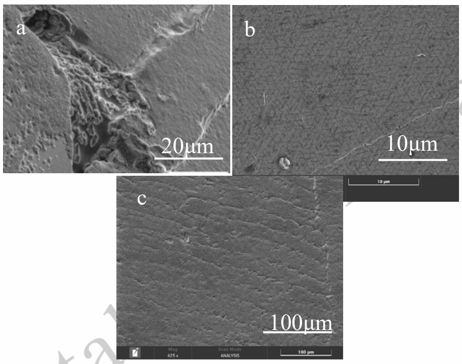

Fig. 14 Sectional enlarged morphology; (a) Crack source area, (b) Microscopic morphology in the first stage of fatigue propagation, (c) Microscopic morphology in the second stage of fatigue propagation

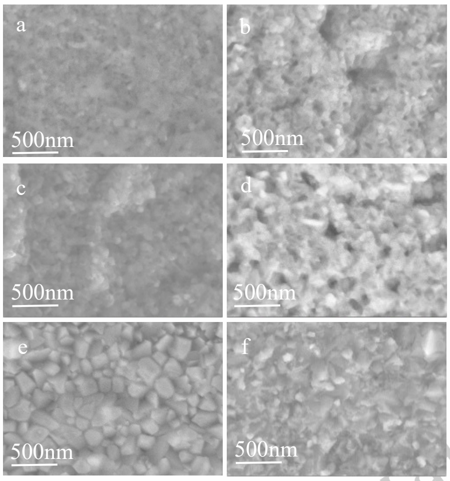

Fig. 15 Corundum-like oxide particles on the surface of (a) sample D1H230 (850 ℃/R = 0.05, σ_{max} = 660 MPa), (b) sample D6H202 (760 ℃/R = 0.05, σ_{max} = 650 MPa), (c) sample D6H203 (760 ℃/ R= -1, σ_{max} = 410 MPa), (d) sample D6H207 (760 ℃/R = -1, σ_{max} = 410 MPa), (e) sample D6H229 (850 ℃/R = -1, σ_{max} = 450MPa), and (f) sample D6H236 (850 ℃/R = -1, σ_{max} = 365 MPa)

Table 8 The EDS component analysis results for the cross-section

D1H230		D6H202		D6H203	
Element	Weight ratio%	Element	Weight ratio%	Element	Weight ratio%
O	17.38	O	20.59	O	23.05
Al	6.34	Al	0.58	Al	2.00
Cr	4.76	Cr	1.71	Cr	2.08
Co	7.66	Co	10.80	Co	8.94
Ni	46.46	Ni	52.75	Ni	48.89
		Mo	0.53	Rb	1.57
Ta	6.28	Ta	2.95	Mo	1.12
W	4.60	W	2.35	W	3.71
D6H207		**D6H229**		**D6H236**	
Element	Weight ratio%	Element	Weight ratio%	Element	Weight ratio%
O	18.80	O	17.99	O	22.08
Cr	0.68	Cr	0.44	Cr	0.54
Co	14.97	Co	20.04	Co	17.13
Ni	58.50	Ni	50.60	Ni	51.95
		Pt	4.18		

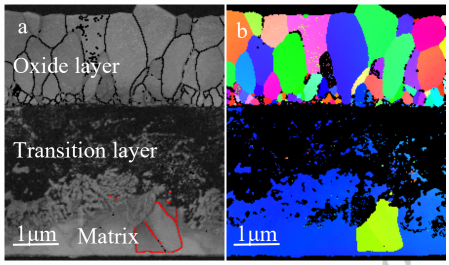

Fig. 16 (a) Sample morphology near the fracture surface; (b) Crystal orientation changes near the fracture surface (Euler angle diagram)

2.3 Acquisition of parameters for the fatigue stress prediction model

1. Solution of the C and n parameter values based on the Paris model

The data processing adopted the seven-point incremental polynomial method. Taking the a-N data, and selecting data point i, based on the data (a_i, N_i) of point i, three consecutive points before and after are added, totaling 7 data points. The corresponding quadratic polynomial for these 7 data points is generated with local fitting using the least squares method[16]:

$$a_i^{\wedge}=b_0+b_1\left(\frac{N_i-C_1}{C_2}\right)+b_2\left(\frac{N_i-C_1}{C_2}\right) \tag{8}$$

and,

$$-1\le\left(\frac{N_i-C_1}{C_2}\right)\le -1 \tag{9}$$

$$C_1=\frac{1}{2}\left(N_{i+3}+N_{i-3}\right) \tag{10}$$

$$C_2=\frac{1}{2}\left(N_{i+3}-N_{i-3}\right) \tag{11}$$

where $a_i^{\wedge}$ represents the fitted crack length, and b_0, b_1, and b_2 denote the regression coefficients determined by the least squares method within the range of $a_{i-3}\le a\le a_{i-3}$.

The crack propagation rate at point N_i can be obtained by differentiating according to Equation (12):

$$\left(\frac{da}{dN}\right)a_i^{\wedge}=\frac{b_1}{C_2}+\frac{2b_2\left(N_i-C_1\right)}{C_2^2} \tag{12}$$

During the stable fatigue crack expansion stage, the Paris model expresses the relationship between the fatigue crack growth rate (da/dN) and ΔK as Equation (1), where C and n represent material constants. Taking the logarithm of both sides gives Equation (13):

$$\lg(\mathrm{d}a/\mathrm{d}N) = \lg c + n\lg(\Delta K) \tag{13}$$

In the double-logarithmic coordinate system, the relationship between da/dN and ΔK is linear, and a linear regression was used to calculate C and n, as shown in Fig. 17.

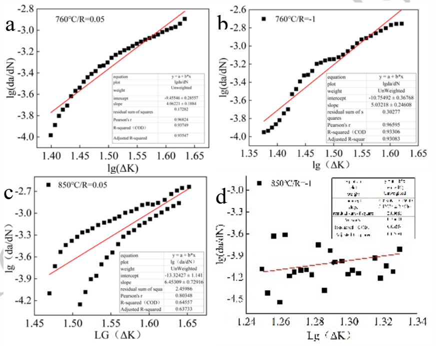

Fig. 17 Linear regression fitting to obtain the Paris model C and n parameters; (a) 760 ℃/R = 0.05; (b) 760 ℃/R = -1; (c) 850 ℃/R = 0.05; (d) 850 ℃/R = -1.

Applying Equation (14), which relates the high-cycle fatigue stress intensity factor (K) to stress and the crack length (a), the fatigue stress prediction model based on the Paris model is presented in Table 9. The da/dN parameter represents crack growth rate (characterized by the fatigue band spacing) with units of mm/cycle. Moreover, a denotes the crack length, given in units of m, K has units of MPa √m, whereas n is a dimensionless parameter. The material constant (C) should be regarded as a dimensional quantity ((-stress intensity factor) -n × crack growth rate units) where the associated units are closely related to the fitted da/dN data and the units of ΔK.

$$\Delta K = \Delta\sigma \cdot Y_{\mathrm{I-II-III}} \cdot \sqrt{\pi a} \tag{14}$$

The second stage of crack stable expansion exhibits visible fatigue bands. Consequently, the expansion formula that can represent the intermediate segment and rapid expansion stage of crack propagation performance is adopted[17]. In addition, the fracture toughness (K_C) and R parameters are considered, employing the Forman model (Equation (2)); R is a known constant, C and n are the experimentally determined crack propagation-related constants, and K_C is the fracture toughness determined by the material and thickness. The K_C parameter was obtained according to the "Mechanical Properties Manual of Materials for Certain Types of Aviation Engines Design".

The determination of the C and n values was based on a fitting of experimental crack propagation results obtained at different temperatures. Applying the crack propagation data at 760 ℃ and 850 ℃ with R=-1 and R=0.05, the Forman model parameters were determined using the logarithmic relationship:

$$\lg\left(\frac{\mathrm{d}a}{\mathrm{d}N}\right) + \lg((1-R)Kc - \Delta K) = \lg c + n\lg(\Delta K) \tag{15}$$

The resultant values of C and n are given in Table 9.

At temperatures of 850 ℃ and 760 ℃, with stress ratios R=-1 and R= 0.05, the associated Forman model Equations are given in Table 9. The units of the model parameters are consistent with those of the Paris model.

As the relationship between da/dN and Δσ is a complex function, it cannot be calculated by a simple manipulation of the component terms. Applying Matlab software, Δσ was calculated; the associated program is presented in Appendix 1.

Table 9 Paris and Forman formula and fatigue stress prediction model

Test conditions	Paris formula stress prediction model	Forman stress prediction model
760 °C/R = 0.05	$C=10^{-9.45\pm0.28}$, n=4.06±0.19, $R^2 = 0.94$	$C=10^{-6.91\pm0.29}$, n=3.63±0.19, $R^2 = 0.92$
760 °C/R = -1	$C=10^{-10.75\pm0.36}$, n=5.03 ±0.25, $R^2 = 0.93$	$C=10^{-9.04\pm0.41}$, n=5.02±0.27, $R^2 = 0.90$
850 °C/R = 0.05	$C=10^{-13.32\pm1.1}$, n=6.45±0.72, $R^2 = 0.64$	$C=10^{-10.6\pm1.1}$,n =5.88±0.72, $R^2 = 0.60$
850 °C/R = -1	$C=10^{-18.02\pm3.16}$, n=3.12 ±2.4, $R^2 = 0.06$	$C=10^{-6.9\pm2.73}$, n=3.99±2.12, $R^2 = 0.12$

2.4 Fatigue stress prediction based on brittle fatigue band spacing

1) Measurement and extraction of fatigue band spacing

Using the fatigue band spacing measurement method outlined in section 2.5, the spacing from the position where the fatigue bands appear on the sample fracture surface to the end position of the bands (the second extension stage) was measured and recorded. The results are presented in Fig. 19 and Table 10. The crack propagation rates under different experimental conditions and different crack lengths measured on the fracture surface are provided in Table 10. At 850 ℃/R = 0.05, the fatigue band spacing is 0.025 mm-0.09089 mm, which compares with 0.02179 mm-0.0942 mm and 0.016 mm-0.16897 mm (at 850 ℃/R =-1), 0.02135 mm-0.0545 mm (at 760 ℃/R = 0.05), and 0.06 mm-0.1575 mm and 0.01368 mm-0.1179 mm (760 ℃/R=-1). The fatigue band spacing in the stable extension zone of the high-cycle fatigue fracture surfaces of steel and Al alloys is in the 1×10^{-4} mm-0.0025 mm range, as shown in Figure 20. When compared with the fracture quantitative map, the fatigue band spacing in the second extension stage of the single crystal alloy is very wide, with a difference of several orders of magnitude. Moreover, there are obvious differences in morphology. The fatigue bands of the high-temperature alloy exhibit concave-convex features and a relatively round shape. The surface of the fatigue bands is relatively flat and sharp, and the characteristics in the later stage of high-cycle fatigue expansion can be defined as "brittle fatigue bands"[18].

2) Crack shape outline and calculation of the composite shape factor

The fatigue bands were subjected to low-magnification analysis at two positions to obtain values of the semi-width axis (c) and the semi-length axis (b) of the semi-elliptical crack, used to calculate the crack shape factor. The ratio of the short axis (c) to the long axis (b) of the crack was calculated, where linear fitting produced c/b values at different crack lengths. As the high-cycle fatigue fracture surface of the nickel-based single crystal superalloy is inclined, the diameter (D) is taken as the longest dimension formed by the fracture surface.

The c/b values at different crack lengths are substituted into the crack shape factor model Equation 7, and the I-type crack shape factors at different crack lengths are obtained. The model is introduced as follows:

The high-cycle fatigue cracks of single-crystal superalloys are typically types I, II, and III. This implies a composite coefficient and the shape factor of the composite cracks must be calculated based on crystal slip theory. The angle α represents the angle between the normal vector of the crack surface (in the [111] direction) and the direction of applied stress (in the [001] direction). The calculated α is 54.7° by applying Equation 16 and the critical plane method[19].

A schematic representation of the rotation between the crystal coordinate axis of the single-crystal superalloy and the actual coordinate axis is shown in Fig. 18, serving as the basis for the Rodrigues' Rotation calculation. The original coordinate system is represented as $\vec{x}=(1,0,0)$, $\vec{y}=(0,1,0)$, $\vec{z}=(0,0,1)$, while the new coordinate system is denoted as $\vec{z}=(1,1,1)$, $\vec{y}=(x_2,y_2,z_2)$, $\vec{x}=(x_3,y_3,z_3)$. The K_{I} parameter corresponds to the stress (σ) generated in the $\vec{x}'$ direction, K_{II} is associated with the shear stress, and K_{III} is related to the shear stress.

The Rodrigues' Rotation formula (Equations (17) and (18)) is used to rotate the crystal coordinate axes. In the first step, the vector $\vec{y}_\alpha'$ is rotated by an angle (α) around the axis defined by (0, -1, 1), resulting in the transformed vector $\vec{y}_\alpha'$. The detailed calculation process has been reported in our previous study[2].

$$\cos\alpha=\frac{[001]\cdot[111]}{|001|\cdot|111|}=\frac{1}{\sqrt{3}} \tag{16}$$

$$\vec{y}_\alpha'=\left(\cos\alpha\begin{bmatrix}1&0&0\\0&1&0\\0&0&1\end{bmatrix}+(1-\cos\alpha)\vec{n}\vec{n}'+\sin\alpha\begin{bmatrix}0&-n_z&n_y\\n_z&0&-n_x\\-n_y&n_x&0\end{bmatrix}\right)\vec{y} \tag{17}$$

Normalizing the rotation axis (0, -1, 1) yields $\vec{n}=\vec{n}$

$$=\begin{bmatrix}0\\-\frac{\sqrt{2}}{2}\\\frac{\sqrt{2}}{2}\end{bmatrix}=\begin{bmatrix}n_x\\n_y\\n_z\end{bmatrix}.$$

In Step 2, the vector $\vec{y}_\alpha'$ is rotated by an angle (η) around the axis $\vec{z}'$ (1, 1, 1) to yield the transformed vector $\vec{y}$.

$$\vec{y}'=\left(\cos\theta\begin{bmatrix}1&0&0\\0&1&0\\0&0&1\end{bmatrix}+(1-\cos\theta)\vec{n}\vec{n}'+\sin\eta\begin{bmatrix}0&-n_z&n_y\\n_z&0&-n_x\\-n_y&n_x&0\end{bmatrix}\right)\vec{y}_\alpha' \tag{18}$$

The superposition of K_{I}, K_{II}, and K_{III} stress intensity factors can be represented using empirical formulas that incorporate material properties[20]. Applying Equation (19), utilizing a coefficient of 1.25 as an empirical value and a second coefficient based on the material Poisson's ratio, the calculated composite stress intensity factor correction coefficient (C) is 0.74. By integrating this correction with the I-type crack shape factor calculation (Equation (20)), we have derived expressions for the shape factors of composite types I, II, and III cracks[21]. The calculated composite crack shape factors for the three samples are provided in Table 10.

$$K_{\mathrm{I-II-III}}=\sqrt{(K_{\mathrm{I}})^2+1.25(K_{\mathrm{II}})^2+4.27(K_{\mathrm{III}})^2}=C\times K_{\mathrm{I}} \tag{19}$$

$$Y_{\mathrm{I-II-III}}=0.74\times\left[\frac{1.81+3.48x_1-2.10x_2-4.82x_1x_2+4.32x_1^2+1.40x_2^2}{\sqrt{1+1.46(x_2)^{1.65}}}\right] \tag{20}$$

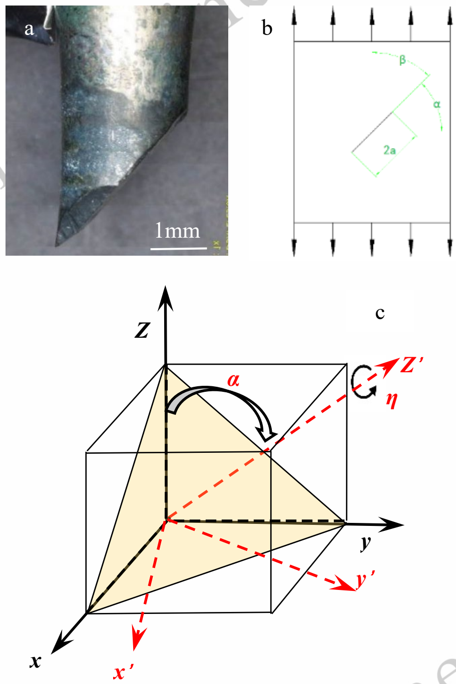

Fig. 18 (a) Sample oblique cracking; (b) Oblique crack model; (c) Schematic representation of crystal slip and angular deflection

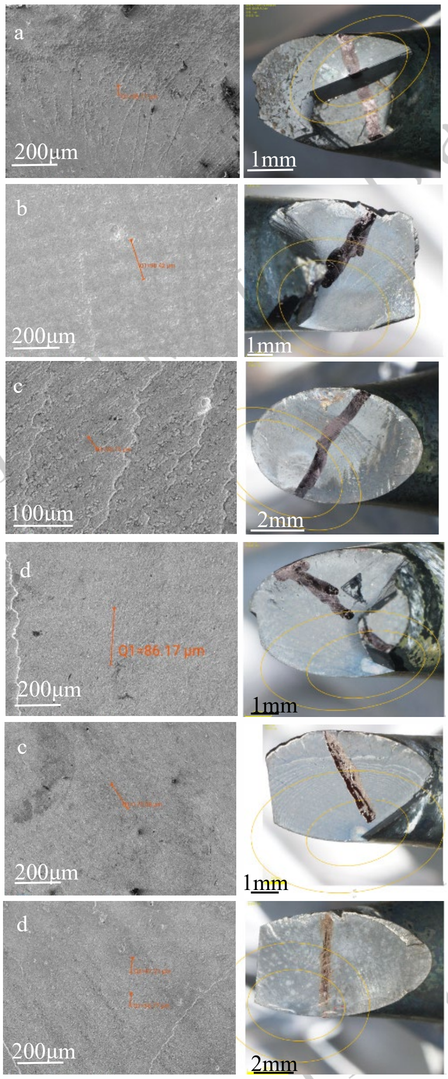

Fig. 19: Measurement of the fatigue band spacing and crack c/b value for (a) sample D1H230 (850 ℃/R = 0.05), (b) D6H229 (850 ℃/R = -1), (c) sample D6H236 (850 ℃/R = -1), (d) sample D6H202 (760 ℃/R = 0.05), (e) D6H203 (760 ℃/R = -1), and (f) sample D6H207 (760 ℃/R = -1)

Table 10 Crack propagation rate (da/dN) at different crack lengths (a) and associated c/b and c/D ratio

D1H230 850 ℃/R = 0.05

a/m	da/dN/mm	c/D	c/b	$Y_{I-II-III}$
0.001142804	0.02500	0.38	0.511	1.29
0.001232234	0.05200	0.41	0.513	1.36
0.001336759	0.06845	0.45	0.511	1.47
0.001441284	0.08090	0.48	0.518	1.55
0.001519704	0.08690	0.51	0.513	1.65
0.001598124	0.09089	0.53	0.521	1.71

D6H229 850 ℃/R = -1

a/m	da/dN/mm	c/D	c/b	$Y_{I-II-III}$
0.002610843	0.02179	0.37	0.7214	0.88
0.002927729	0.03399	0.42	0.7101	0.99
0.003125412	0.04521	0.45	0.7043	1.06
0.003360015	0.06680	0.48	0.6985	1.14
0.003545007	0.07950	0.51	0.6900	1.22
0.00373	0.09420	0.53	0.6909	1.29

D6H236 850 ℃/R = -1

a/m	da/dN/mm	c/D	c/b	$Y_{I-II-III}$
0.00139	0.01600	0.28	0.497	1.07
0.001689083	0.01979	0.29	0.493	1.10
0.001899737	0.02313	0.30	0.489	1.13
0.002016383	0.03015	0.31	0.485	1.16
0.002163793	0.04023	0.34	0.476	1.27
0.002120849	0.06900	0.35	0.476	1.27
0.002441065	0.08690	0.38	0.469	1.38
0.002468299	0.16897	0.40	0.464	1.46

D6H202 760 ℃/R = 0.05

a/m	da/dN/mm	c/D	c/b	$Y_{I-II-III}$
0.001661	0.02135	0.42	0.5497	1.29
0.001912	0.03057	0.48	0.5496	1.47
0.001995	0.04309	0.50	0.5496	1.53
0.002094	0.04899	0.52	0.5496	1.61
0.002262	0.05450	0.57	0.5496	1.74

D6H203 760 ℃/R = -1

a/m	da/dN/mm	c/D	c/b	$Y_{I-II-III}$
0.00236	0.06	0.39	0.63	1.07
0.00278	0.086	0.46	0.64	1.23
0.00310	0.11074	0.52	0.64	1.36
0.00340	0.13412	0.57	0.64	1.51
0.00369	0.1575	0.62	0.64	1.65

D6H207 760 ℃/R = -1

a/m	da/dN/mm	c/D	c/b	$Y_{I-II-III}$
0.00253	0.01368	0.42	0.79	0.86
0.00267	0.01272	0.45	0.80	0.90
0.00274	0.01679	0.46	0.80	0.91
0.00306	0.02905	0.51	0.82	1.00
0.00330	0.06199	0.55	0.82	1.06
0.00365	0.11790	0.61	0.83	1.18

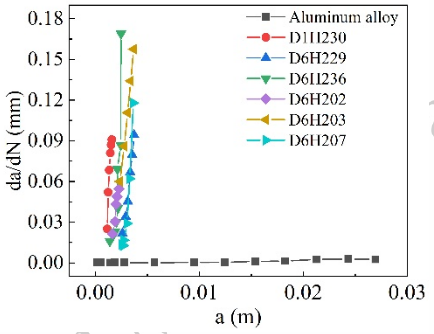

Fig. 20 Comparison of the expansion rates of single-crystal high-temperature alloys and aluminum alloys

3) Fatigue stress prediction based on the Paris and Forman models

The measured fatigue strip spacing (da/dN) and crack shape factor ($Y_{I\text{-}II\text{-}III}$) were substituted into the fatigue stress prediction model based on the Paris formula (Table 9). The extended stress calculation results from the second-stage fracture extension were compared with the stress range ($\Delta\sigma$) applied to the corresponding tested samples. According to established formulas, the predicted fatigue fracture stress corresponds to a stress range $\Delta\sigma$ that is converted into σ_{max}. The error range associated with the fatigue stress calculated using the inverse method for different samples and the different crack lengths (a) is from 1.04 to 1.96.

$$\sigma_{\max} = \frac{\Delta\sigma}{1-R} \tag{21}$$

In addition, the da/dN and $Y_{I\text{-}II\text{-}III}$ data were substituted into the Forman model (in Table 9) for fatigue stress prediction. The resultant calculated fatigue stress error range is from 1.00 to 1.30. All the results are shown in Table 11 and Fig. 21.

As the da/dN and $\Delta\sigma$ represent a complex functional relationship[22], Matlab software was used to calculate the stress ($\Delta\sigma$), as outlined in Appendix 1.

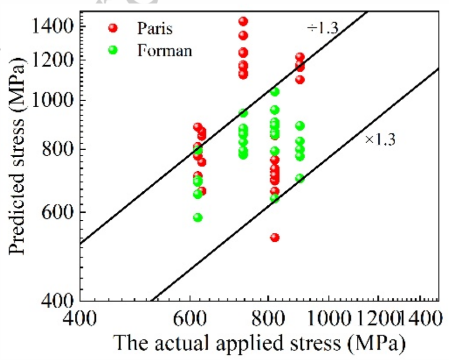

Fig. 21 Fatigue stress prediction error based on the Paris and Forman models.

2.5 Fatigue stress prediction based on brittle fatigue band spacing

1) Crystallographic analysis of slip cracking behavior

Nickel-based single-crystal alloys exhibit a face-centered cubic structure. The schematic presented in Fig. 22 illustrates the slip planes associated with octahedral and hexagonal slip systems[21]. In terms of crystal slip theory, nickel-based single crystal high-temperature alloys mainly activate octahedral and hexagonal slip systems at temperatures below 980 ℃. Applying Equations (22) and (23), the magnitude of shear stress in the hexagonal slip system is independent of the normal stress in the crystal coordinate system and only depends on the shear stress. In the case where the loading direction coincides with the principal axis of the crystal coordinate system, the normal stress is significantly greater than the shear stress, and the shear stress in the hexagonal slip system is much smaller than that in the octahedral slip system[23,24]. Consequently, when the structure loading mainly occurs along the principal axes, only the octahedral slip system has to be considered. This is consistent with the crystal orientation of the fracture surface in Fig. 12.

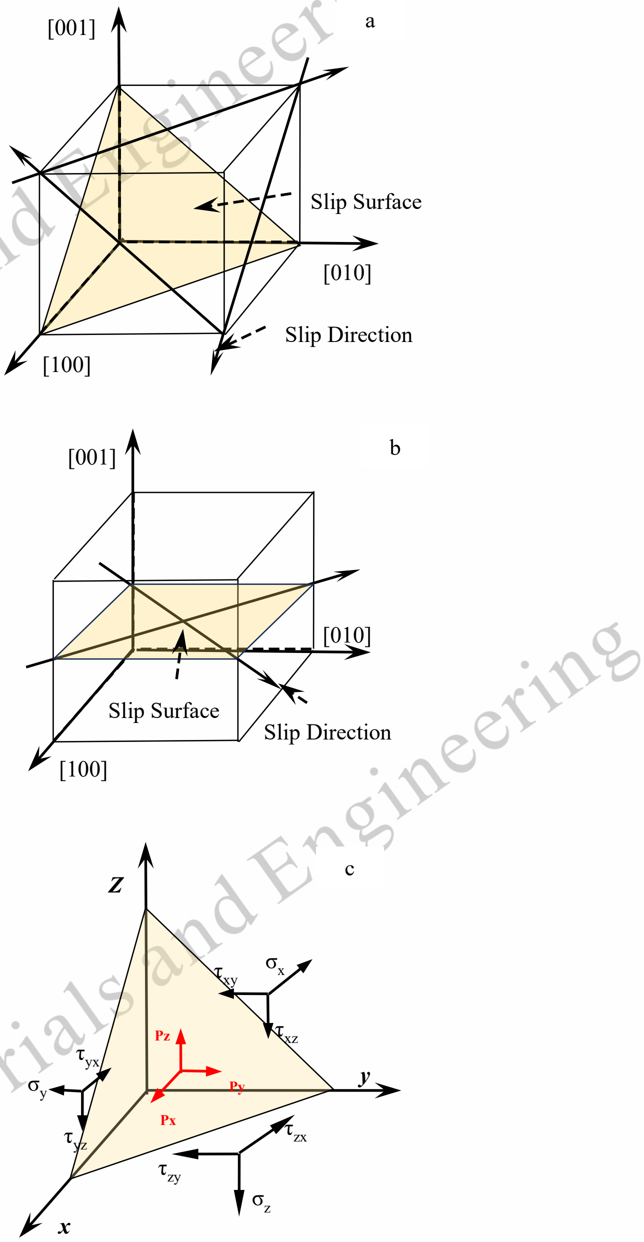

Fig. 22 (a) {1,1,1} slip surface and slip direction for the octahedral slip system; (b) {0,0,1} slip surface and slip direction for the hexagonal slip system; (c) Schematic representation of the material micro-element

$$\pi_1^o=(p_x,p_y,p_z)\bullet(\frac{\sqrt{2}}{2},0,-\frac{\sqrt{2}}{2})=\frac{\sqrt{2}}{2}(p_x-p_z)$$
$$=\frac{\sqrt{2}}{2}\bullet\frac{\sqrt{3}}{3}(\sigma_{x'}+\tau_{y'x'}+\tau_{z'x'}-\tau_{x'z'}-\tau_{y'z'}-\sigma_{z'})=\frac{1}{\sqrt{6}}(\sigma_{x'}+\tau_{y'x'}-\tau_{y'z'}-\sigma_{z'})$$

Octahedral slip system (22)

$$\pi_1^c=\vec{p}\bullet\overrightarrow{m_1^c}=(p_x,p_y,p_z)\bullet(\frac{\sqrt{2}}{2},\frac{\sqrt{2}}{2},0)=\frac{\sqrt{2}}{2}(\tau_{z'x'}+\tau_{z'y'})$$

Hexagonal slip system (23)

2) Slip behavior, microstructural dislocations on the main slip plane {111} and the formation of the "slip plane" at the fracture surface

The dislocation morphology associated with the main slip plane during crack propagation is shown in Fig. 23(a). The dislocations are mostly in the form of long and straight dislocation lines arranged in pairs (in parallel). These are accompanied by a secondary component of arc-shaped dislocations. An appreciable number of dislocation heads and tails are evident at the interface of the γ'/γ strengthening phase particles. The resultant pile-up contributes to shear or particle bypass. This response represents a typical planar slip feature[25].

At medium and low temperatures or high strain rates, dislocation movement is restricted by the stacking fault energy. This energy is low in the case of nickel-based single crystal alloy, with a consequent wide dislocation extension that changes direction from the original slip plane. Consequently, dislocations tend to move on a single {111} slip plane and accumulate at obstacles (such as the γ' phase) or in the channels. This is consistent with the theoretical analysis provided above[26].

At the early stage of fatigue crack propagation, the stress intensity factor range (ΔK) is small, and the plastic zone at the crack tip is negligible. The deformation on the {111} slip plane is principally formed by the reciprocating motion of dislocations on the slip system, forming a stationary slip zone. The crack slowly shears and extends along these slip zones. At this point, the material exhibits good cyclic plasticity, and fatigue bands are not evident on the fracture surface in the first stage of fatigue expansion, but the slip plane characteristics are present[27].

In the later stage of crack propagation, dislocations exhibit a longer dislocation size with a zigzag shape. Cross slip occurs and a dislocation network is formed, which is the result of damage accumulation, as shown in Fig. 23(c).

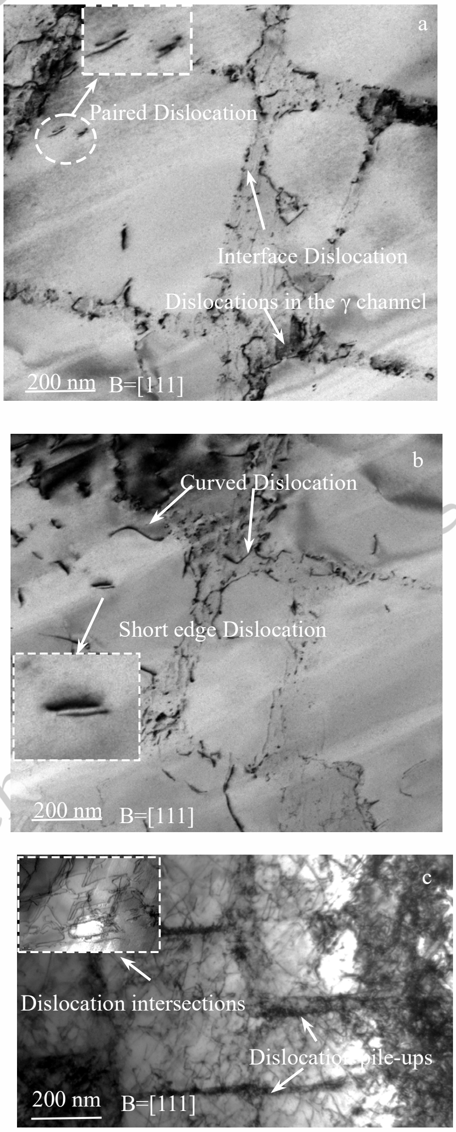

Fig. 23 (a) Paired Dislocation in the γ' strengthened phase and γ channel; (b) Short edge dislocation in the γ' strengthened phase and γ channel; (c) Dislocation morphology in the brittle fatigue band region

3) The formation mechanism of the "brittle fatigue band" in the second stage of fatigue crack propagation

The micro-dislocation and slip configuration mechanism for the main slip surface is illustrated in Fig. 24. During crack propagation, the size of the dislocations increases and the dislocation morphology becomes diverse with more dislocation blockages and entanglements. The dislocation movement switches from planar slip to cross slip and climbing. The mode of dislocation cutting the γ' phase changes from regular slip to localized shear. The high stress at the crack tip in the later stage of crack propagation combined with the cumulative temporal damage results in a quasi-fracture-like "jump" propagation model, where the cross-section presents a "brittle fatigue band"[28]. When the stress intensity factor (K_{max}) approaches K_c in the later stage of crack propagation, the "brittle fatigue band" feature becomes more distinct. The crack tip changes from continuous plastic slip to an intermittent quasi-fracture[28]. We also observed this phenomenon of ductile-to-brittle transition on the fracture surface of the samples in the fatigue crack propagation test, as shown in Fig. 25.

Polycrystalline materials such as steel and aluminum alloys exhibit relatively good toughness, and crack propagation largely occurs *via* repeated passivation-reactivation at the crack tip [29]. This process results in appreciable plastic deformation, and the fatigue bands are fine and continuous. As a result of the ordered strengthening phase, anisotropy, and the effects of high temperature and cumulative damage in single crystal superalloys, the crack propagation is dominated by a fracture-like mode. This represents a "leaping" form of expansion, with limited plastic deformation, so the bands are wide and discontinuous, exhibiting a clear outline and "brittle" characteristics. As a consequence of this brittle characteristic, the degree of fracture expansion in each cycle is greater, and the spacing of the toughness bands exceeds that of steel and aluminum alloys[30].

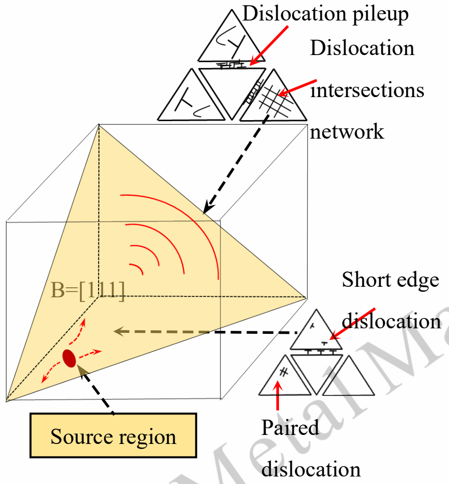

Fig. 24 Single crystal high-temperature alloy slip transformation mechanism

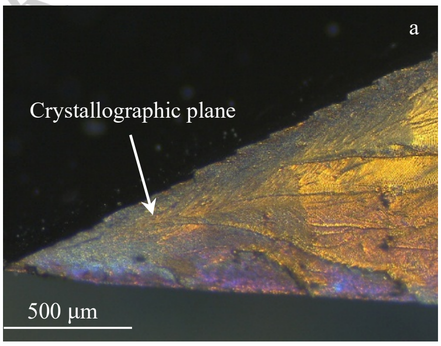

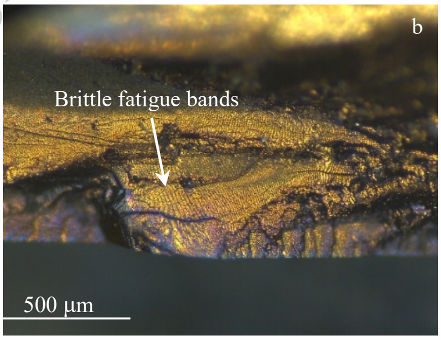

Fig. 25 Characteristics of (a) the initial slip plane, and (b) later stage brittle fatigue bands

4) Effect of environmental temperature and crack tip damage on surface oxidation

The thickness of the oxidation layer formed at 850 °C is significantly higher than that recorded at 760 °C (Table 12). The environmental temperature has a significant impact on the degree of fracture oxidation. The thickness of the oxidation layer varies at different crack lengths on the same sample, and the oxidation layer thickness in the crack propagation zone is significantly higher than that in the crack initiation zone[31].

There is no obvious regularity with respect to the differences in the layer thickness for different stress ratios at the same temperature. The oxide layer thickness varies at different crack lengths for the same sample, and the oxide layer thickness in the crack propagation zone is significantly higher than that in the crack initiation zone. Oxide formation is not only related to the temperature but is also affected by the initiation position. In the case of high-cycle fatigue samples, initiation and propagation predominantly take place internally. Consequently, the source is not the position that first comes into contact with the environment and the supply of oxygen. This is significantly different from the samples where cracks are initiated and propagate from the outer surface[32]. In addition, the oxide formation is related to the degree of damage and deformation at the fracture surface and below the crack as it is propagated. The plastic zone at the crack tip and the stress intensity factor at the crack tip gradually increase, accompanied by section oxidation. The initiation area, the associated exposure time in the high-temperature environment, and the degree of oxidation are different. During crack fatigue extension, microscopic grinding between sections results from an opening and closing of the crack with a consequent increase in temperature and oxidation. The results demonstrate that the contribution of the plastic zone at the crack tip is significant with respect to the damage of the material matrix and the level of oxidation [33].

Table 12 The thickness of the oxide layer near the crack source and in the expansion zone

Sample number	Near the source/μm	The extension area/μm
D6H202 (760 ℃/R=0.05)	0.18	0 (Oxide layer peeling)
D1H230 (850 ℃/R=0.05)	0.27	2.13

D6H203 (760 ℃/R=-1)	0.09	0 (Oxide layer peeling)
D6H207 (760 ℃/R=-1)	0.57	0.8
D6H229 (850 ℃/R=-1)	0.87	1.09
D6H236 (850 ℃/R=-1)	0.34	0.73

2.6 Comparison and Analysis of Errors in the Forman and Paris Models

As noted in section 3.4.3, the calculation error factor for predicted fatigue stress using the Paris model ranges from 1.04 to 1.96, and the range in the case of the Forman model is 1.00 to 1.30. The principal objective of the fatigue fracture stress prediction is to establish a physical characteristic of the fracture surface that reflects the crack propagation rate and underpins the fatigue stress prediction model. When the characteristics of the fracture surface do not match the model, a large error results. The Paris model is used to describe the crack propagation of a stable crack extension. Fatigue bands appear in the case of polycrystalline alloys, which facilitate the application of this model. However, brittle fatigue bands appear in the later stage of fatigue crack propagation in single crystal superalloys. A comparison of results has shown that the prediction error for the Paris model is significantly greater than that of the Forman model. This indicates that the fracture characteristics do not match the stress prediction model[34].

The development of fatigue cracks can be divided into crack initiation, stable propagation, and rapid propagation stages. The general fatigue crack propagation rate curve (Fig. 26) exhibits three straight lines with different slopes: the near-threshold region, the stable propagation region, and the rapid propagation region. The near-threshold region is associated with the low-rate stage of fatigue crack propagation with an associated threshold value (ΔK_{th}) for fatigue crack propagation. Where $\Delta K < \Delta K_{th}$, the crack does not propagate. In the stable propagation region, the rate of fatigue crack propagation is significantly lower than that achieved in the final stage (rapid propagation region). The lifetime is significantly shorter and the crack size increases rapidly[35-37].

Nickel-based single crystal high-temperature alloys have a high yield strength, but the fracture toughness (K_C) is relatively low, especially in the later stage of crack propagation. The Forman model incorporates R and K_C to ensure that the model effectively captures the entire process of crack propagation.

In the later stage of crack propagation, when K_{max} approaches K_C, the crack tip enters the critical state and the crack propagation rate increases sharply. The Forman model effectively reflects this "acceleration effect" in the denominator term ($(1-R)K_C-\Delta K$). However, the Paris model fails to capture the influence of R. The change in value of R during high-cycle fatigue directly affects crack opening and the residual stress field. Where R = -1 and R = 0.05, the difference in the crack closure effect is significant. The Forman model corrects this influence *via* the R term and improves the prediction accuracy[38,39].

The classic Paris model is effective in predicting the fatigue stress for high-cycle fatigue fracture in polycrystalline materials such as steel and aluminum. As such, it provides valuable support for failure analysis and fault detection in engineering practice. However, the Paris model exhibits serious limitations in fatigue stress prediction and reverse calculation when applied to single crystal superalloys. The Paris model is a simple power function relationship, which relies on ΔK to express fatigue crack propagation. It ignores such key influences as stress ratio and material fracture toughness, resulting in an inability to predict the acceleration phenomenon in the later stages. In the high-speed expansion zone, the model underestimates the actual ΔK or stress level, leading to inaccurate fatigue stress prediction. Consequently, it is essential to select the fatigue stress prediction model that is based on the characteristics of the alloy and the particular fatigue fracture features.

Using the Monte Carlo simulation method, the standard deviation of the stripe spacing (±5%) was taken as the input variable to evaluate the impact on the stress predictions of the Paris and Forman models. The results have shown that the Forman model is less sensitive to measurement errors, with an error amplification coefficient of approximately 1.2. The Paris model has a coefficient of approximately 1.8. This indicates that the Forman model exhibits better robustness[40].

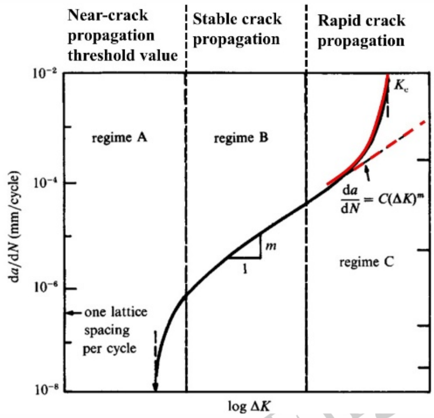

Fig. 26 Representation of the three crack propagation stages based on rate

3 Conclusions

1) At temperatures of 760 ℃ and 850 ℃, the fracture characteristics of high-cycle fatigue at stress ratios (R) = 0.05 and -1 are similar, and consistent with typical staged features. The cracks all originate from internal voids in the material. The early stage of crack propagation exhibits smooth and flat crystallographic plane characteristics. In the later stage, a "brittle fatigue band" feature is observed. The fracture surface is at an angle (ranging from 50° to 60°) to the direction of load

application, and constitutes a composite crack.

2) The characteristics of the brittle fatigue bands in the later stage of fatigue propagation have been quantitatively analyzed. At 760 ℃ and 850 ℃, R = 0.05 and -1, the crack propagation rate response is similar. The spacing of the fatigue bands is in the 0.01368-0.16897 mm range. The crack propagation rate differs significantly (by several orders of magnitude) from that observed for polycrystalline materials. This is related to the transformation of the single-crystal high-temperature alloys from a plastic slip mechanism to an intermittent quasi-slip plane fracture mechanism.

3) Fatigue crack propagation tests were conducted under appropriate temperature and stress ratio conditions, and the parameters required for the fatigue stress prediction model were calculated. It is necessary to select an appropriate "cylindrical semi-elliptical surface crack" shape factor, and calculate the correction coefficient of the composite crack shape factor.

4) The Bowman model R and K_C parameters can be used to accurately predict fatigue stress. The Paris model has certain limitations when applied to single-crystal high-temperature alloys. The fatigue fracture stress prediction serves to establish a fatigue stress prediction model corresponding to the physical characteristics that represent the surface crack propagation rate. The resultant mathematical model incorporates physical features. Large errors are the result of a mismatch between the model and the fracture surface characteristics.

5) The findings of this research can inform an assessment of the actual service stress from the high-cycle fatigue fracture surface in engineering applications. A combination of the crack propagation threshold value (ΔK_{th}) and fracture toughness (K_C) enables a determination of the maximum allowable initial defect size for the blade material. This can provide a basis for non-destructive testing standards in the casting and processing processes. Moreover, the approach taken can support decisions on extending the lifespan and blade remanufacturing, thereby reducing operating costs.

References

1 Shen Z , Chen C , Xuan H . *Engineering failure analysis*[J], 2024, 163(Part A):108414.

2 Li Z , Xu Y M , Liu X L *et al. Engineering Failure Analysis*[J], 2025, 170(Part A):109166.

3 Xu J C , Zhao X B , Chen J S *et al. International Journal of Plasticity*[J], 2025,184:104207.

4 Zhou H G , Luo H Y. *Materials Science and Engineering, A* [J].2025, 922:147596.

5 Zhang J G, Liu X L, C X *et al. Rare Metal Materials and Engineering*[J],2024, 53(9):2458-2467.

6 Yang D Y, Zhou L, Wen Y *et al. Materials Science Forum*[J],2013 (23):564-568.

7 Zhang W F , Gao W, Zhao, A G *et al. Journal of Mechanical Strength*[J], 2003,25(4), 436-440.

8 Li H Y, Zhang X R, Yang X J *et al. Chinese Journal of Aeronautics*[J], 2001, 22(4):303-307.

9 Zheng Z T, You Y L, Liu X L *et al. Journal of Materials Engineering*[J], 2013, (11): 50 -56.

10 Cheng X , Lu Z W, Hu C J. *Failure Analysis and Prevention*[J], 2016, 11(4):277-280.

11 Tan L , Yang X G , Shi D Q ,*et al. International Journal of Fatigue*[J], 2025, 190:108619.

12 Cui Z, Liu M P, Zeng Y *et al. Rare Metal Materials and Engineering*[J],2024,53(8):2375-2389.

13 Li L Y, Tian F Z, Li Z *et al. Rare Metal Materials and Engineering*[J], 2024, 53(7):1874-1881.

14 China Aeronautics Research Institute (1993). *Stress intensity factor handbook. Beijing*[M]*: Science Press* :786-789.

15 Tarpani J R, Ruckert C, Milan M T *et al. Engineering Failure Analysis* [J], 2004,11(4):547-559.

16 Wang C, Wang X, Yu H *et al. Rare Metal Materials and Engineering*[J],2024,53(1):113~123.

17 Yang H C, Fan J K, Song Y L *et al. Chinese Journal of Rare Metals*[J],2024, 48(9):1274-1291.

18 Zhang Z F, Wang W H , Jiang R S, *et al. International Journal of Mechanical Science*[J]. 2022, 229:107514.

19 Yaren M F , Ayhan A O. *Theoretical and Applied Fracture Mechanics*[J], 2024,131:104355.

20 Liu X L, Zhang Z, Tao, C H. (2010). *Fatigue fractography quantitative analysis*[M]. National Defense Industry Press:158-182.

21 Wang R Q , Jing F L, Hu D Y *et al. Journal of Aerospace Power*[J] 2013,28(11):2587-2592.

22 Leidermark D , Moverare J, Simonsson K *et al. International Journal of Fatigue*[J],2011,33(10):1351-1359.

23 Xie H J, Li J R, Han M. *Rare Metal Materials and Engineering*[J],2018,47(11):3381-3386.

24 Li Z, Liu X L, Chen X *et al. Rare Metal Materials and Engineering*[J],2020,49(8):2730~2737.

25 Liu X L, Zhang W F, Tao C H. *Journal of Mechanical Engineering Materials*[J] 2008,32(5):12-15.

26 Hadipour A , Jafari Eskandari M , Gholami M G *et al. Journal of Failure Analysis and Prevention*[J], 2024, 24(2).

27 Li Z , Xu Y M , Liu X L *et al. Metals* 2024, 14(12), 1354.

28 Wang C, Yang L, Sheng R X *et al. Journal of Materials Research and Technology*[J],2025,36,1511-1521.

29 Su H , Wang C , Luo T et al. *Rare Metal Materials and Engineering*[J],2024, 53(7):2006-2017.

30 Wang J, Huang H L , Xin D *et al. Journal of Materials Research and Technology*[J], 2024,30,1950-1961.

31 Hao Z H, Zhang Z, Wu S J, et al. *Journal of Mechanical Strength*[J],2008,30 (3):385-391.

32 Wu K , Li K , Hao L L *et al. Engineering Failure Analysis*[J], 2025, 167(PartA):108955.

33 Zhang D, Zhong P D, Tao C H (2004). *Failure analysis*[M]. National Defense Industry Press:55-61.

34 Wang R Q, Li K, Hu D Y. *Journal of Aerospace Power*[J],2017,32(3):677-682.

35 Pan X N , Hong Y S, *International Journal of Fatigue*[J], Aug.2024,186:108226.

36 Xia B , Wang B , Zhang P *et al. International Journal of Fatigue*[J], 2022,161:106891.

37 Yi C, Shen S Z. Journal of Harbin Institute of Technology[J], 2000, 33(5): 55-112.

38 Application of fracture mechanics (2012). *Beijing University of Aeronautics and Astronautics Press*[M]:15-95.

39 Hu C Y, Liu X L, Tao C H *et al. Rare Metal Materials and Engineering*[J]. 2019,48(10):3190-3194.

40 Qin, R Y, Zhou T, Sun B B, *et al. Failure Analysis and Prevention*[J],2024, 19(1): 1-5.

Table 11 Fatigue stress prediction results based on the Paris and Forman model

D1H230 850 ℃/R = 0.05

a/m	da/dN/mm	Experimental applied stress Δσ/MPa	Paris model predicted stress Δσ/MPa	Error calculation	Forman model predicted stress Δσ/MPa	Error calculation
0.001142804	0.02500	627	848.38	1.35	817.46	1.30
0.001232234	0.05200	627	868.15	1.38	817.90	1.30
0.001336759	0.06845	627	804.71	1.28	750.99	1.20
0.001441284	0.08090	627	754.28	1.20	699.12	1.12
0.001519704	0.08690	627	697.73	1.11	645.70	1.03
0.001598124	0.09089	627	661.11	1.05	609.74	1.03

D6H229 850 ℃/R = -1

a/m	da/dN/mm	Experimental applied stress Δσ/MPa	Paris model predicted stress Δσ/Mpa	Error calculation	Forman model predicted stress Δσ/MPa	Error calculation
0.002610843	0.02179	900	1217.63	1.35	889.64	1.01
0.002927729	0.03399	900	1174.43	1.30	829.99	1.08
0.003125412	0.04521	900	1160.60	1.29	798.88	1.13
0.003360015	0.06680	900	1175.84	1.31	774.06	1.16
0.003545007	0.07950	900	1126.56	1.25	729.75	1.23
0.00373	0.09420	900	1098.07	1.22	699.40	1.29

D6H236 850 ℃/R = -1

a/m	da/dN/mm	Experimental applied stress Δσ/MPa	Paris model predicted stress Δσ/MPa	Error calculation	Forman model predicted stress Δσ/MPa	Error calculation
0.00139	0.01600	730	1246.17	1.71	942.84	1.29
0.001689083	0.01979	730	1175.18	1.61	870.82	1.19
0.001899737	0.02313	730	1132.56	1.55	825.79	1.13
0.002016383	0.03015	730	1163.36	1.59	825.94	1.13
0.002163793	0.04023	730	1122.47	1.54	779.55	1.07
0.002120849	0.06900	730	1342.03	1.84	878.93	1.20
0.002441065	0.08690	730	1237.25	1.69	794.52	1.09
0.002468299	0.16897	730	1431.60	1.96	855.07	1.17

D6H202 760 ℃/R = 0.05

a/m	da/dN/mm	Experimental applied stress Δσ/MPa	Paris model predicted stress Δσ/MPa	Error calculation	Forman model predicted stress Δσ/MPa	Error calculation

0.001661	0.02135	617.5	884.64	1.43	796.38	1.29
0.001912	0.03057	617.5	790.45	1.28	694.38	1.12
0.001995	0.043085	617.5	809.06	1.31	687.70	1.11
0.002094	0.04899	617.5	774.61	1.25	651.23	1.05
0.002262	0.05450	617.5	707.93	1.15	585.65	1.05

D6H203　760 ℃/R＝-1

a/m	da/dN/mm	Experimental applied stress Δσ/MPa	Paris model predicted stress Δσ/MPa	Error calculation	Forman model predicted stress Δσ/MPa	Error calculation
0.00236	0.06000	820	850.86	1.04	1039.69	1.27
0.00278	0.08600	820	732.57	1.12	890.15	1.09
0.00310	0.11074	820	659.77	1.24	792.92	1.03
0.00340	0.13412	820	589.57	1.39	705.94	1.16
0.00369	0.15750	820	534.60	1.53	638.51	1.28

D6H207　760 ℃/R＝-1

a/m	da/dN/mm	Experimental applied stress Δσ/MPa	Paris model predicted stress Δσ/MPa	Error calculation	Forman model predicted stress Δσ/MPa	Error calculation
0.00253	0.01368	820	762.06	1.08	956.54	1.17
0.00267	0.01272	820	698.66	1.17	886.65	1.08
0.00274	0.01679	820	720.76	1.14	904.15	1.10
0.00306	0.02905	820	692.17	1.18	865.12	1.06
0.00330	0.06199	820	731.06	1.12	890.93	1.09
0.00365	0.11790	820	709.56	1.16	853.17	1.04

镍基单晶高温合金在高周疲劳断裂机制与疲劳应力预测模型

李振[1,2,3,4]，徐元铭[2]，刘新灵[1,3,4]，陈星[1,3,4]，刘昌奎[1,3,4]

(1. 中国航发北京航空材料研究院，北京　100095)

(2. 北京航空航天大学，航空科学与工程学院，北京，100191)

(3. 航空材料检测与评价北京市重点实验室，北京 100095)

(4. 中国航发/中航工业失效分析中心，北京 100095)

(5. 中国航空发动机集团材料检测与评价重点实验室，北京 100095)

摘　要：开展了不同温度下镍基单晶高温合金的高温高周疲劳试验，运用光学显微镜和扫描电子显微镜对高周疲劳断口进行宏/微观观察，总结了镍基单晶高温合金高周疲劳疲劳断裂特征，开展了对应条件下的疲劳裂纹扩展试验，获取了稳定扩展特性，最终建立了新的疲劳断口定量分析参量和疲劳应力预测模型，并对试样承受的高周疲劳应力进行预测，对比计算了不同模型误差。结果表明：760 ℃、850 ℃，应力比 R=0.05、-1 条件下的高周疲劳裂纹萌生位置、扩展方向、断面特征相似，呈现典型的阶段性特征；裂纹均起源于材料内部疏松空洞处，裂纹扩展区前期为光滑平整的晶体学平面特征，裂纹扩展区后期可见“脆性疲劳条带”特征；断面与载荷施加方向呈一定角度，为复合型裂纹。镍基单晶合金的“脆性疲劳条带”特征与钢、铝多晶合金在形貌上、间距尺寸数量级存在明显不同，根据获取的疲劳裂纹稳定扩展阶段特性，计算得到疲劳应力预测模型所需的参数；选用体现镍基单晶高温合金高周疲劳裂纹萌生、扩展走向的裂纹形状因子“圆柱半椭圆表面裂纹”，计算体现表征合金斜裂纹特点的复合型裂纹形状因子修正系数；分别选用传统 Paris 模型和考虑循环特性应力比 R、断裂韧性 K_{IC} 的 Forman 模型的疲劳应力预测模型进行应力预测，将预测结果与名义应力进行比对计算误差；Paris

模型预测误差倍数在 1.0~1.9，Forman 模型预测误差在 1.05~1.30；表明疲劳应力预测需选择与疲劳断口特征匹配的疲劳应力预测参量和应力预测模型。

关键词：镍基单晶高温合金；高周疲劳；裂纹萌生机理；脆性疲劳条带；复合型裂纹；裂纹形状因子；疲劳应力预测；损伤容限设计

作者简介：李振，男，1995 年生，博士研究生，工程师，中国航发北京航空材料研究院，北京 100095，电话：17310379975，E-mail: 18753365060@163.com

Appendix 1: Matlab Program for Solving Forman Formula

```
clc;clear
S = xlsread('D6H206-prais.xlsx','A2:A13');
N = xlsread('D6H206-prais.xlsx','B2:B13');
C = xlsread('D6H206-prais.xlsx','C2:C13');
y = xlsread('D6H206-prais.xlsx','D2:D13');
A = xlsread('D6H206-prais.xlsx','E2:E13');
r = xlsread('D6H206-prais.xlsx','F2:F13');
KC = xlsread('D6H206-prais.xlsx','G2:G13');
%%
clc
syms x
list = ones(12,1);
outlist = ones(12,1);
for i=1:12
    s = S(i,1);
    n = N(i,1);
    c = C(i,1);
    Y = y(i,1);
    a = A(i,1);
    R = r(i,1);
    Kc = KC(i,1);
    right_up = c * ((x * Y * (pi * a)^0.5))^n;
    right_down = (1 - R) * Kc - (x * Y * (pi * a) ^ 0.5);
    left = s;
    solx = vpasolve((right_up) / (right_down) == left , x);
    a = solx;
    list(i,1) = a;
end
xlswrite('Table1.xlsx',list,'Sheet1','A1:A12')
disp('Write successful!');

%%
for i=1:12
s = S(i,1);
n = N(i,1);
```

```
c = C(i,1);
Y = y(i,1);
a = A(i,1);
R = r(i,1);
Kc = KC(i,1);
x = list(i,1)
right_up = c * ((x * Y * (pi * a)^0.5))^n;
right_down = (1 - R) * Kc - (x * Y * (pi * a) ^ 0.5);
output = right_up/right_down;
disp(output)
outlist(i,1)=output;
end
```